Supporting Information

Structural Tuning of $BiVO_4$/MnFe-MOF Photoanodes Boosts Hole Extraction for Photoelectrochemical Water Splitting

Chenchen Feng[a]*, Longyue Liu[a], Houyu Fu[a], Faqi Zhan[a] , Henan Jia[a], Xiang Cheng[c], Fucheng Yu[a], Qi Zhou[a], Zongkun Bian[a]*, Beibei Zhang[b]*

[a] School of Materials Science and Engineering, State Key Laboratory of Advanced Processing and Recycling of Non-ferrous Metals, Lanzhou University of Technology, Lanzhou 730050, China.

[b] Institute of Fundamental and Frontier Sciences, University of Electronic Science and Technology, Chengdu 610054, China.

[c] College of Science, Hebei Agricultural University, Baoding 071001, China

Experiments section

1. Materials

Bismuth nitrate pentahydrate ($Bi(NO_3)_3·5H_2O$, 99%), Manganese sulphate monohydrate ($MnSO_4·H_2O$, 99%), Ethanol, potassium hydroxide (KOH) and sodium hydroxide (NaOH) were purchased from Sinopharm Chemical Reagent Co, Ltd. Vanadium oxyacetylacetonate ($VO(acac)_2$), boric acid (H_3BO_3) and quinone hydroquinone ($C_{12}H_{10}O_4$) were purchased from Shanghai Aladdin Biochemical Technology Co, Ltd. 2,5-Dihydroxyterephthalic acid, potassium iodide (KI), ferrous sulfate heptahydrate ($FeSO_4·7H_2O$), dimethyl sulfoxide (DMSO) and N,N-dimethylformamide were purchased from Shanghai Maclean's Biochemicals Co, Ltd, Tianjin Beilian Chemical Industry Co., Ltd, Yantai Shuangshuang Chemical Industry Co, Ltd, Xilong Science and Technology Co, Ltd, and Lianlong Bohua (Tianjin) Pharmaceutical and Chemical Co, Ltd, respectively. Unless otherwise indicated, all reagents are analytically pure and do not require further purification. Deionized water with a resistivity of 18.25 MΩ·cm (25 °C) was used during all experiments. The fluorine-doped tin oxide (FTO, 1 × 2.5 cm^2) conductive glass was cleaned by sonication in acetone, isopropanol, ethanol, and deionized water for 30 min before use.

2. Synthesis of photoanodes

2.1 Preparation of nanoporous $BiVO_4$ photoanodes

A solution was prepared by adding 1.66 g of KI to 25 mL of deionized water and stirring until completely dissolved. Subsequently, 0.485 g of $Bi(NO_3)_3 \cdot 5H_2O$ was added to the dissolved solution, and stirring was continued for 30 min. Once stirring was completed, HNO_3 was added to adjust the pH of the solution. The solution was then stirred for a further three hours, after which it was noted as A. The addition of 0.27 g of quinone hydroquinone to 10 mL of ethanol and stirring for three hours resulted in the creation of solution B. This was then added to solution A and stirred for 30 minutes to obtain the electrodeposited solution. In the electrodeposition process, a three-electrode electrolytic cell was used for the deposition, in which FTO was used as the working electrode (1 × 2.5 cm^2, WE), Ag/AgCl was used as the reference electrode (RE), and Pt sheet electrode was used as the counter electrode (CE). The BiOI electrode (1 × 1 cm^2) was obtained by deposition for 5 min at room temperature and constant potential (- 0.1 V vs. Ag/AgCl). Subsequently, a DMSO solution of 0.2 M $VO(acac)_2$ was formulated for coating the electrode. Thereafter, 100 μL of the solution was dispensed dropwise on the BiOI electrode, which was then subjected to calcination in a muffle furnace at a rate of 2 °C/min for 2 h at 450 °C. This procedure resulted in the conversion of BiOI to $BiVO_4$. Finally, the calcined electrode was immersed in a 1 M NaOH solution for 30 min to remove any residual V_2O_5 from the electrode surface. Following this, the electrode washed and dried with deionized water to obtain the nanoporous $BiVO_4$ photoelectrode.

2.2 Decoration with MnFe-MOF catalysts on $BiVO_4$ photoanodes

48 mg of 2,5-dihydroxyterephthalic acid, 78 mg of $FeSO_4 \cdot 7\ H_2O$ and 13 mg of $MnSO_4 \cdot H_2O$ were added to 25 mL of N,N-dimethylformamide, stirred for 3 h, and then sonicated for 1 h. The BiVO4 photoanode prepared in the previous step was then immersed in a 50 mL Teflon-lined steel autoclave containing the above solution, followed by heat treatment at 140 ℃ for 20 h. The PEC activity of the photoanode was optimized by adjusting the reaction time, temperature and Mn:Fe ratio. After allowing the stainless-steel autoclave to cool naturally to room temperature, the sample was removed and rinsed with deionized water. Finally, the $BiVO_4$/MnFe-MOF photoanode material was obtained by drying at 60 ℃. For $BiVO_4$/Mn-MOF and $BiVO_4$/Fe-MOF photoanodes, only $MnSO_4 \cdot H_2O$ and $FeSO_4 \cdot 7H_2O$ were added.

3. Characterization

Scanning electron microscope (SEM) images were acquired using a SU8020 (Hitachi) with an acceleration voltage of 1 kV. Transmission electron microscopy (TEM) and Element distribution mapping (EDS) images were obtained using a Tecnai TF20 (FEI) with an acceleration voltage of 200 kV. X-ray diffraction (XRD) patterns were recorded by Smartlab-SE (Rigaku) with Cu Kα radiation under 40 kV. X-ray photoelectron spectroscopy (XPS) measurements were performed on an Escalab 250XI (Thermo) with an excitation source of Mg Kα, and all the spectra were calibrated by the C1s peak at 284.8 eV. The Fourier transform infrared (FT-IR) spectra were obtained using a Nexus 670 spectrometer to analyze the chemical bond information. UV-vis diffuse reflectance spectra were collected from a UV-2550 spectrometer with $BaSO_4$ as the reference. Photoluminescence spectra (PL) were measured by a fluorescence spectrophotometer (F-7100FL).

4. Photoelectrochemical measurements

An electrochemical workstation (CHI 660D) was used for photoelectrochemical testing of the prepared photoelectrode materials. In a standard three-electrode system, Ag/AgCl (saturated KCl) is used as the reference electrode (RE), a platinum sheet is used as the counter electrode (CE), and the prepared photoelectrode (1×1 cm^2) is used as the working electrode (WE). The light source was a 300 W Xe arc lamp (Beijing Perfectlight Technology Co. Ltd., Microsolar 300D) equipped with an AM 1.5G filter, with an incident light intensity of 100 mW cm^{-2}, and the electrolyte was 0.5 M K_3BO_3 (pH=9.5). The photocurrent vs. voltage (J-V) characteristics were measured using a linear sweep voltammogram (LSV) with a sweep potential of -0.6 ~ 0.7 V (vs. Ag/AgCl) and a sweep rate of 10 mV s^{-1}.

The Ag/AgCl potential was converted to a reversible hydrogen electrode potential (RHE) by the following equation:

$$E_{RHE} = E_{Ag/AgCl} + 0.0592pH + 0.197\ V\ (25\ ^{\circ}C)$$

Where pH is the electrolyte pH and $E_{Ag/AgCl}$ is the is the potential measured by the experiment.

The Mott-Schottky measurements were performed at a frequency of 1000 Hz (amplitude of 5 mV) in the voltage range of 0.7 ~ 1.2 V_{RHE} and in the dark state. Based on the Mott-Schottky curves, the charge carrier density (N_d) could be calculated by the following equation:

$$N_d = \frac{2}{e\varepsilon\varepsilon_0} \times \left(\frac{dv_s}{d\left(\frac{1}{c^2}\right)} \right)$$

where the electron charge (e) is 1.6 × 10^{-19} C, ε_0 (8.86×10^{-12} F m^{-1}) represents vacuum permittivity, and the relative permittivity of $BiVO_4$ is 68. C is the space charge capacitance in the semiconductor (obtained from the Mott-Schottky curves), and v_s is the Mott-Schottky curve applied potential.

The incident photon current efficiency (IPCE) was determined in a standard three-electrode system with 0.5 m K_3BO_3 electrolyte at 1.23 V_{RHE} using a full solar simulator (Beijing NBeT, 71SW 302) and a motorized monochromator The IPCE result was calculated using the equation:

$$IPCE(\%) = \frac{1240 \times I(\frac{mA}{cm^2})}{P_{light}(\frac{mW}{cm^2}) \times \lambda(nm)} \times 100$$

Where I is the measured photocurrent density at a specific wavelength, λ is the wavelength of incident light and P_{light} is the measured light power density at that wavelength.

The applied bias photon-to-current efficiency (ABPE) of the photoanode was calculated by following equation:

$$ABPE(\%) = \frac{I(\frac{mA}{cm^2}) \times (1.23 - V_{bias})(V)}{P_{light}(\frac{mW}{cm^2})} \times 100$$

where I represent the photocurrent density, V_{bias} is the applied bias, P_{light} represents the incident illumination power density.

The electrochemical impedance spectroscopy (EIS) measurements were carried out in the light and in 0.5 M K_3BO_3 aqueous solution and 0.8 V (vs. RHE) in the frequency range 10^{-1} ~ 10^5 Hz with an AC amplitude of 10 mV. The measured spectra were fitted with Z-view software.

Adding 0.2 M Na_2SO_3 into the 0.5 M K_3BO_3 electrolyte can greatly inhibit the recombination of surface charge carriers on the surface of the photoanode. The surface charge injection efficiency ($\eta_{injection}$) can be determined as following:

$$\eta_{injection} = \frac{J_{H_2O}}{J_{Na_2SO_3}}$$

Where J_{H_2O} and $J_{Na_2SO_3}$ are the photocurrent densities for PEC water oxidation and Na_2SO_3 oxidation, respectively.

The light-harvesting efficiencies (η_{LH}) of $BiVO_4$, $BiVO_4$/Mn-MOF, $BiVO_4$/Fe-MOF and $BiVO_4$/MnFe-MOF were calculated from the following equation:

$$\eta_{LH} = 1 - 10^{-A}$$

The absorbance (A) was obtained from UV−vis diffuse reflection spectroscopy.

The charge separation efficiency ($\eta_{separation}$, the yield of photogenerated holes that have reached the semiconductor/ electrolyte interfaces) of $BiVO_4$, $BiVO_4$/Mn-MOF, $BiVO_4$/Fe-MOF and $BiVO_4$/MnFe-MOF photoanodes were calculated using the following equation:

$$\eta_{separation} = \frac{J_{Na2SO3}}{J_{abs}}$$

The maximum possible photocurrent, J_{abs} is estimated using the standard solar spectrum and the measured absorbance of the photoelectrode as:

$$J_{abs} = \frac{q}{hc}\int_{\lambda 1}^{\lambda 2} \frac{(mm)}{1240(V\,nm)}\phi(\lambda)\eta_{LH}d\lambda$$

where $\phi(\lambda)$ is the AM 1.5G photon flux in units of $Wm^{-2}\cdot nm^{-1}$ (provided by the National Renewable Energy Laboratory, USA), and $A(\lambda)$ is the absorbance at different wavelengths estimated by UV-vis measurements.

The Faradaic efficiency can be determined as:

$$\eta_{O_2} = \frac{4Fn_{O_2}}{Q}$$

$$\eta_{H_2} = \frac{2Fn_{H_2}}{Q}$$

Where η_{O_2} and η_{H_2} is the Faraday efficiency, F is Faraday constant (96485 $C\cdot mol^{-1}$), n_{O_2} and n_{H_2} is the production of hydrogen and oxygen (mol), Q is the number of charges generated by photocarriers (C).

5. DFT calculation

All spin-polarized density functional theory calculations were performed using the Vienna ab initio simulation package (VASP).[1] We employed the projector augmented wave (PAW)

method[2] and pseudopotentials to describe ion-electron interactions, and used the Perdew-Burke-Ernzerhof (PBE)[3] generalized gradient approximation (GGA)[3] to describe electron-electron interactions. Van der Waals interactions were treated using the DFT-D3 method.[4] The initial structures were obtained from the Materials Project.[5] To investigate surface reactions, slab models with a vacuum region of 15 Å were constructed, with bottom atoms fixed at bulk positions. During optimization, the plane wave cutoff energy was set to 500 eV, energy convergence criteria were set to 1e - 5 eV, and force convergence criteria were set to 0.03 eV $Å^{-1}$. Brillouin zone integrations were performed using the Gamma-point grid.

6. Supplemental Figures and Discussions

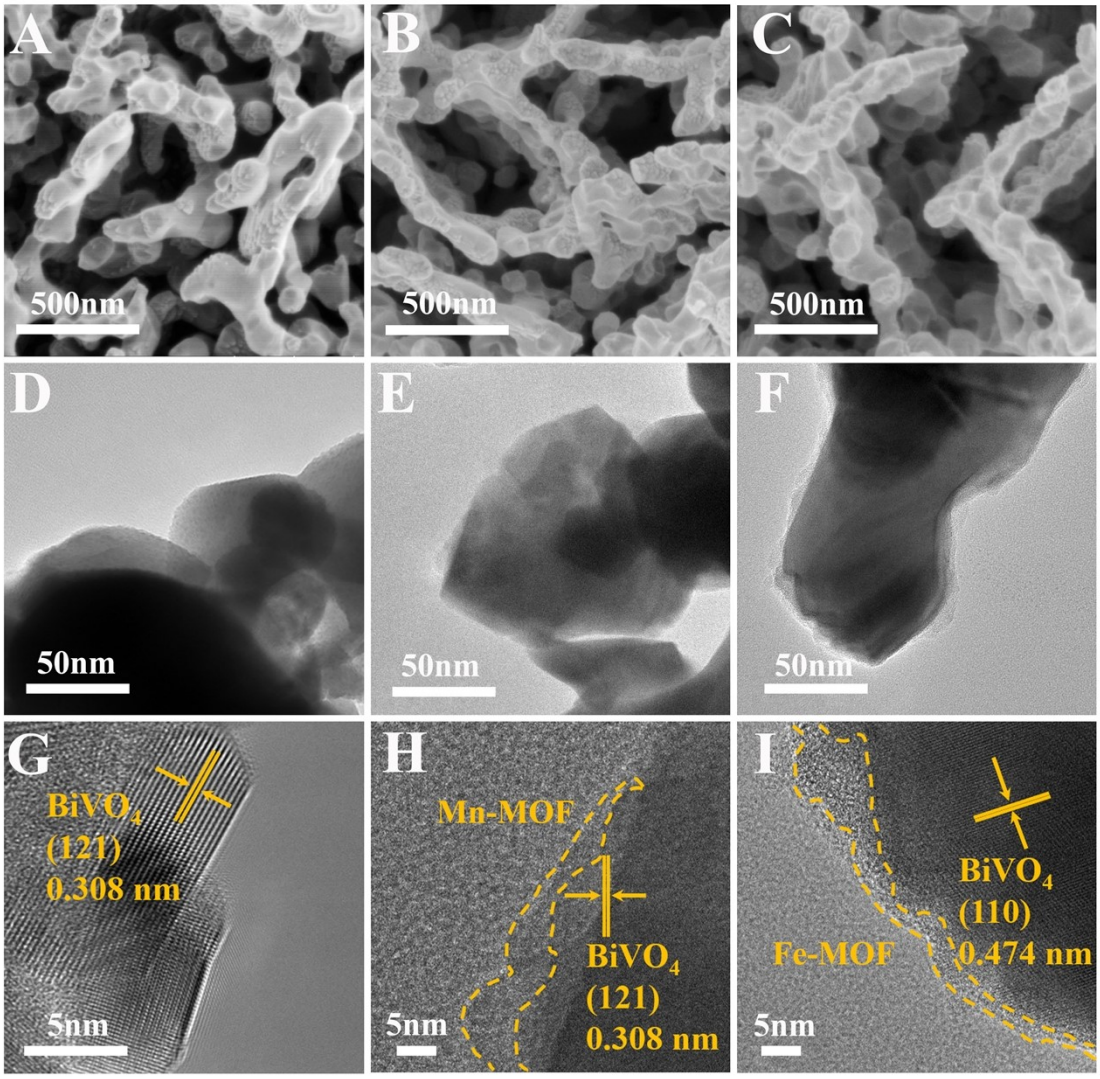

Figure S1. SEM images of $BiVO_4$ (A), $BiVO_4$/Mn-MOF (B) and $BiVO_4$/Fe-MOF (C) photoanodes. TEM images of $BiVO_4$ (D), $BiVO_4$/Mn-MOF (E) and $BiVO_4$/Fe-MOF (F). HR-

TEM images of $BiVO_4$ (G), $BiVO_4$/Mn-MOF (H) and $BiVO_4$/Fe-MOF (I).

Additional discussions

The pure $BiVO_4$ film presents a worm-like structure with smooth surface, and it grows uniformly on the FTO. Its diameter is about 200-300 nm. In contrast, $BiVO_4$/Fe-MOF and $BiVO_4$/Mn-MOF have relatively rough surfaces. Through high-resolution transmission electron microscopy (TEM) images, an uneven island distribution was observed on the surface of $BiVO_4$/Mn-MOF and $BiVO_4$/Fe-MOF, indicating that Mn-MOF and Fe-MOF load on the surface of $BiVO_4$.

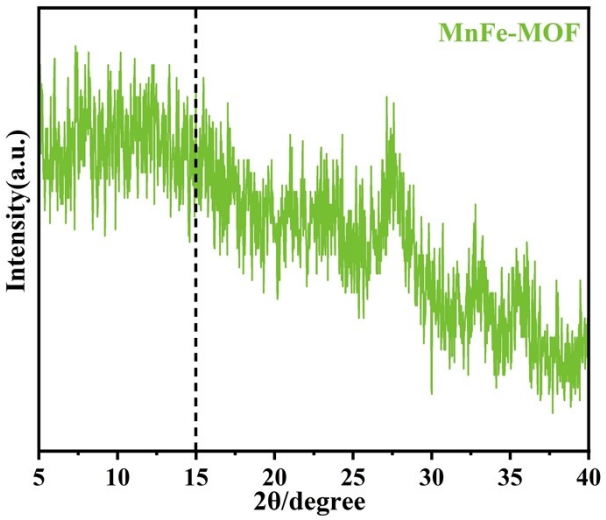

Figure S2. XRD pattern of MnFe-MOF.

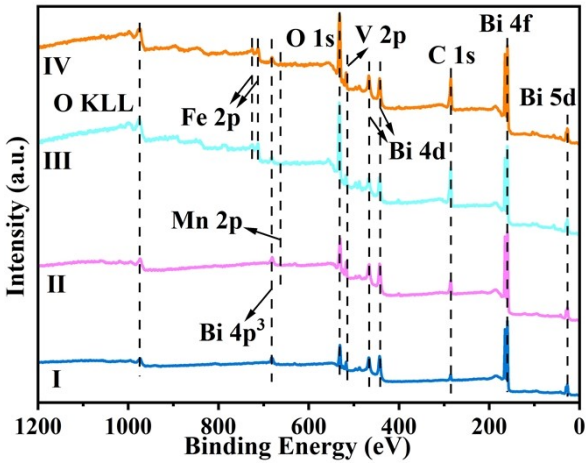

Figure S3. Full-scan XPS spectrum of (I) $BiVO_4$, (II) $BiVO_4$/Mn-MOF, (III) $BiVO_4$/Fe-MOF, (IV) $BiVO_4$/MnFe-MOF.

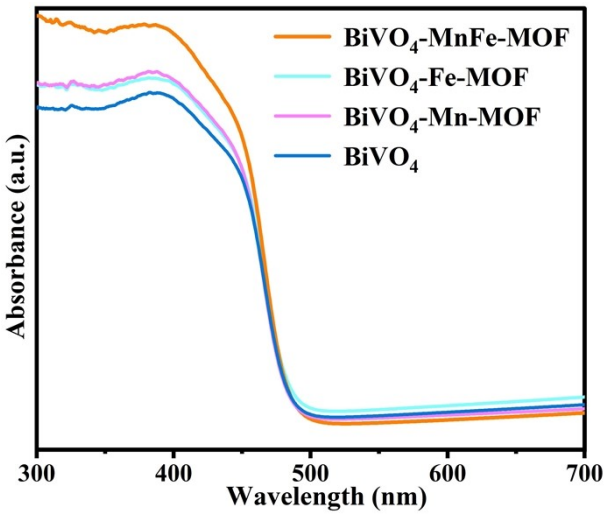

Figure S4. UV-vis diffuse reflectance spectra of $BiVO_4$, $BiVO_4$/ Mn-MOF $BiVO_4$/ Fe-MOF and $BiVO_4$/ MnFe-MOF.

Additional discussions

The optical properties of the as-prepared photoanodes have been explored by ultraviolet-visible (UV-vis) diffuse reflectance spectra. Compared with the pristine $BiVO_4$ photoanode, no evident change could be observed on the MOF catalysts modified $BiVO_4$ samples, suggesting the negative effect of light absorption variations on the significant enhancement of PEC performance.

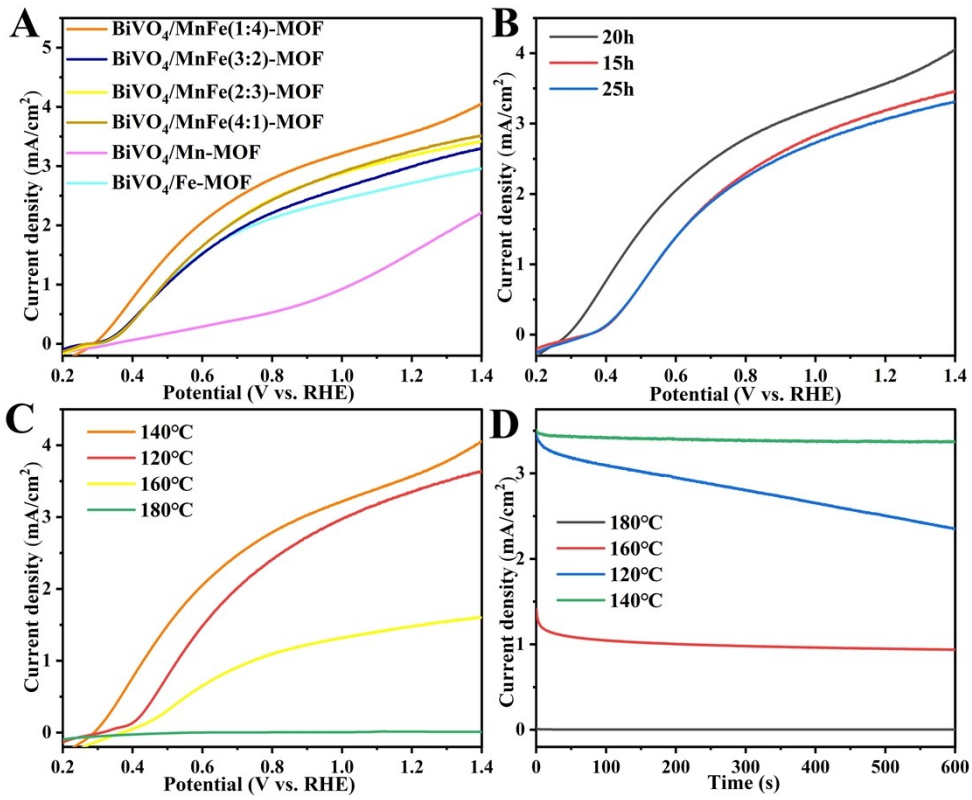

Figure S5. (A) LSV curves at different proportions under light, (B) LSV curves at different times under light, (C) LSV curves at different temperatures under light, (D) i-t curves.

Additional discussions

The PEC activity of $BiVO_4$ photoanode can be enhanced by different proportions of MnFe-MOF. When the MnFe ratio is 1:4, the highest PEC activity is displayed. The photocatalytic activity of anode was investigated by adjusting the hydrothermal time. The PEC activity was better than that of 15h and 25h when the hydrothermal time was 20 h.The effect of hydrothermal reaction temperature on PEC activity of photoanode, among which the photocatalytic activity is the highest at 140℃. By comparing the i-t diagram at 1.23 V_{RHE}, it can be seen that the stability of the reaction temperature is very poor at 120℃, which is attributed to the fact that the surface of the low reaction temperature does not form a uniform coating.

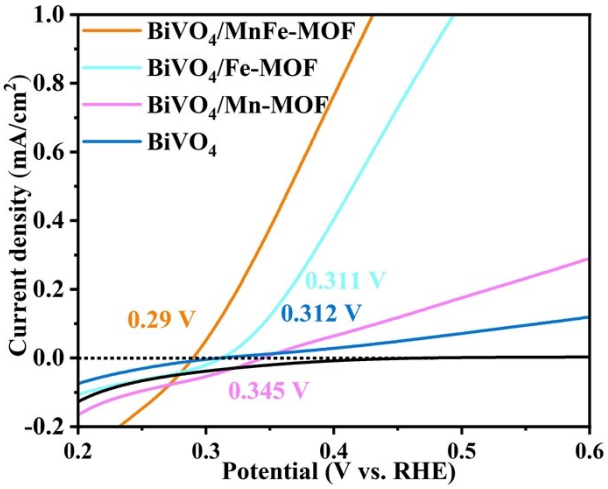

Figure S6. Partially enlarged LSV of $BiVO_4$, $BiVO_4$/Fe-MOF, $BiVO_4$/Mn-MOF, and $BiVO_4$/MnFe-MOF photoanodes.

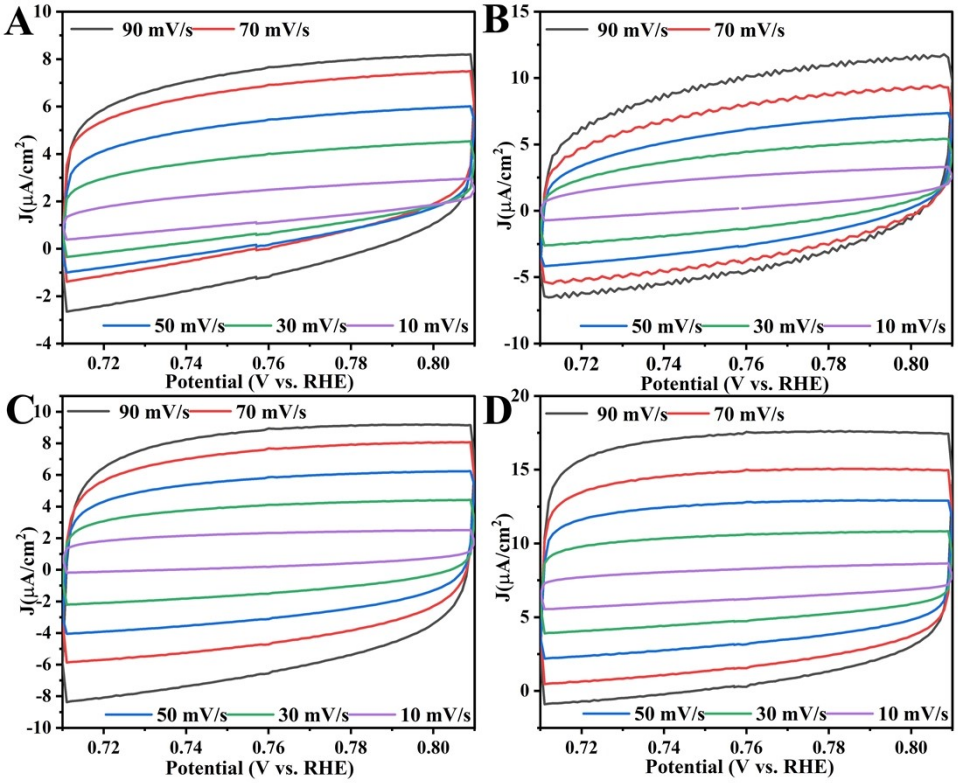

Figure S7. CV curves of $BiVO_4$ (A), $BiVO_4$/ Mn-MOF (B), $BiVO_4$/ Fe-MOF (C) and $BiVO_4$/MnFe-MOF(D), photoanodes at different scanning rates.

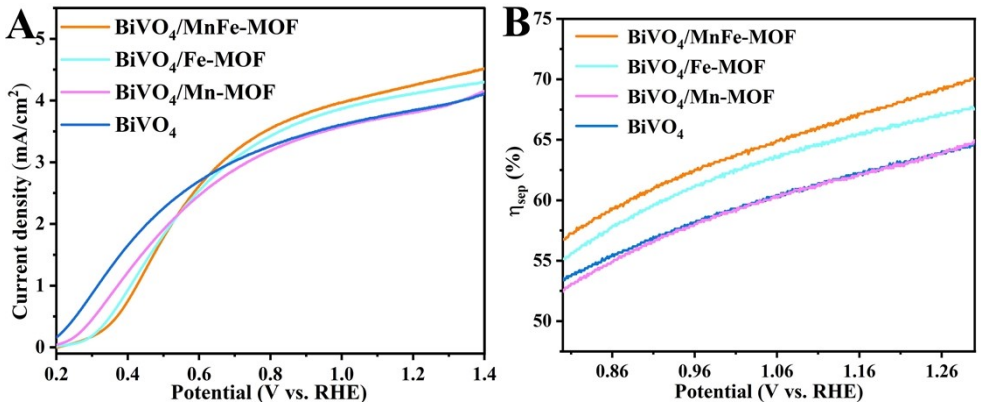

Figure S8. LSV curves measured in 5 M K_3BO_3 contained 0.5 M Na_2SO_3.

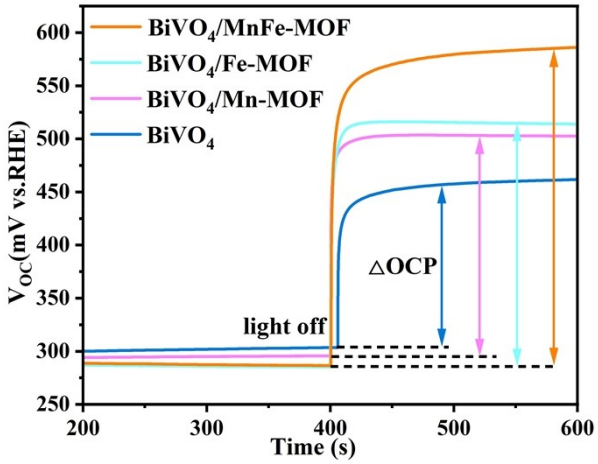

Figure S9. Open-circuit potential (OCP) profiles of iVO_4, $BiVO_4$/ Mn-MOF $BiVO_4$/ Fe-MOF and $BiVO_4$/ MnFe-MOF photoanodes.

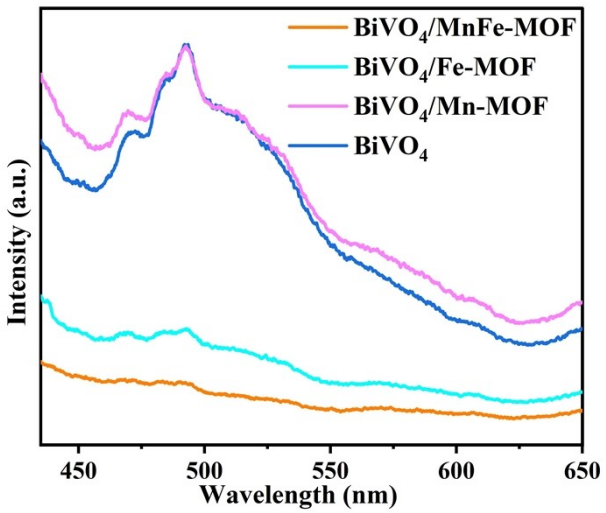

Figure S10. Steady-state photoluminescence (PL) spectra.

Additional discussions

The original $BiVO_4$ showed the strongest PL peak intensity of all the photoanodes, indicating the highest electron-hole recombination rate. After $BiVO_4$ surface modification of MnFe-MOF catalyst, its luminescence peak decreased significantly.

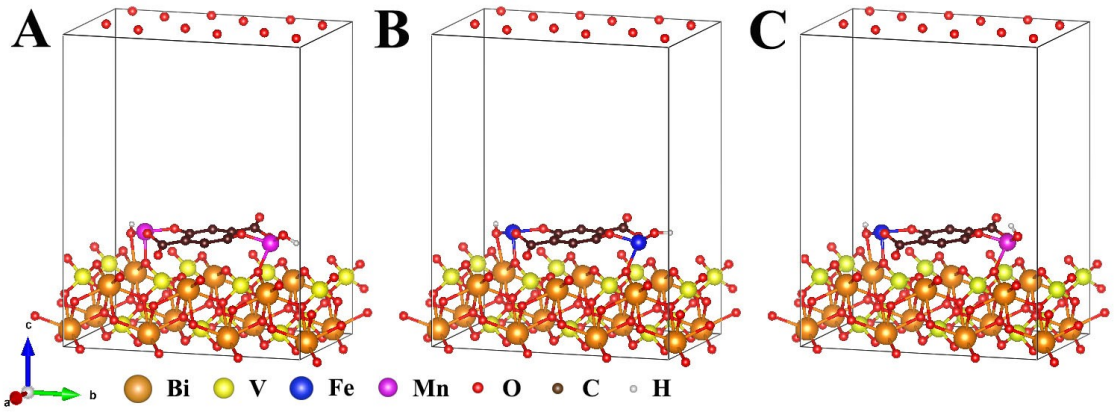

Figure S11. The optimized atomic structure models of $BiVO_4$/Mn-MOF (A), $BiVO_4$/Fe-MOF (B) and $BiVO_4$/MnFe-MOF (C).

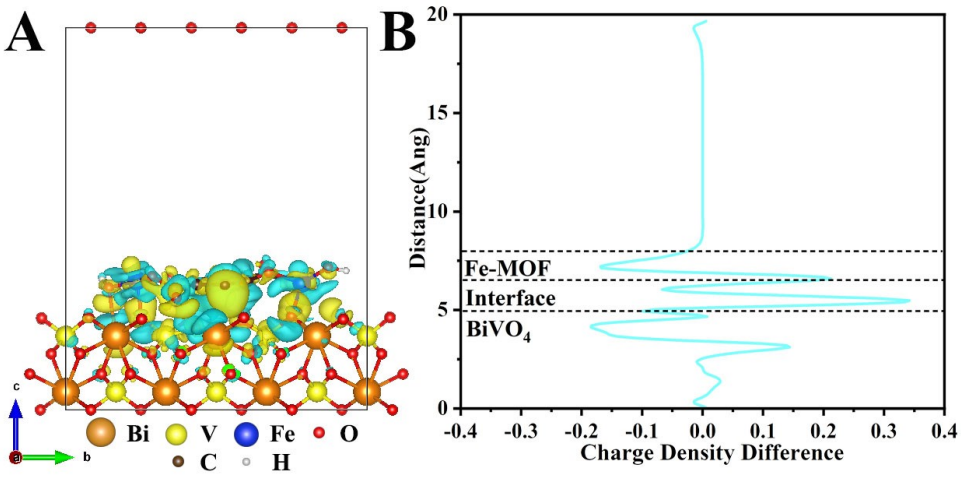

Figure S12. (A) The simulated charge density difference of $BiVO_4$/Fe-MOF, the yellow and blue regions correspond to electron accumulation and depletion, respectively. (B) Charge density difference curves of $BiVO_4$/Fe-MOF along the c-axis.

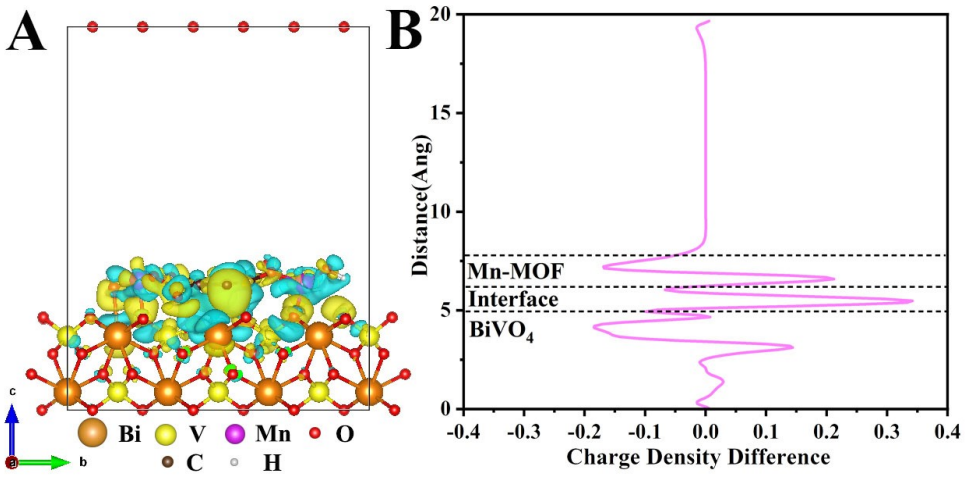

Figure S13. (A) The simulated charge density difference of $BiVO_4$/Mn-MOF, the yellow and blue regions correspond to electron accumulation and depletion, respectively. (B) Charge density difference curves of $BiVO_4$/Mn-MOF along the c-axis.

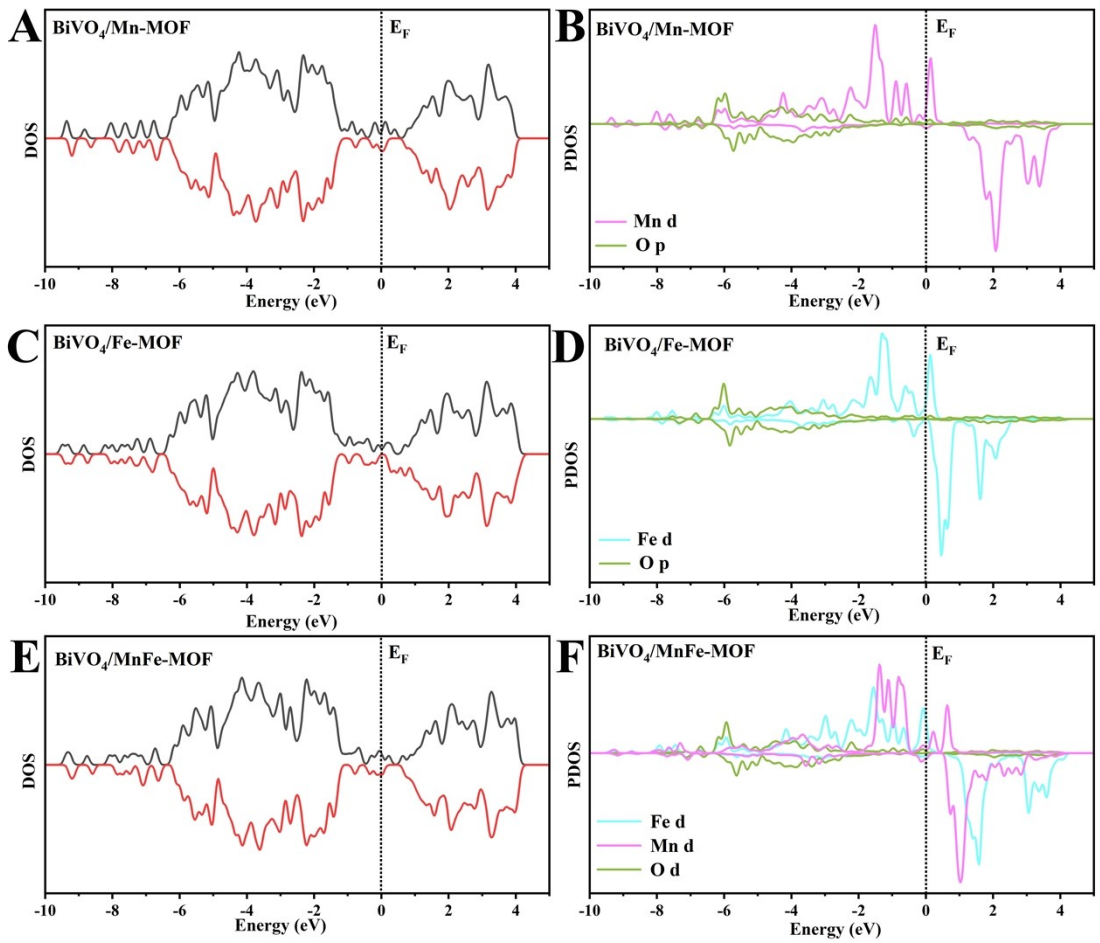

Figure S14. Total DOSs (left) and PDOSs (right) of $BiVO_4$/Mn-MOF (A, B), $BiVO_4$/Fe-MOF (C, D) and $BiVO_4$/MnFe-MOF (E, F).

Additional discussions

Peaks close to the Fermi energy level are visible in the TDOS, indicating favorable metallic characteristics that are conducive to charge transfer. It is evident from the PDOS that the d-orbitals of Fe or Mn predominate close to the Fermi energy level. There is a considerable hybridization between the p-orbitals of O and the d-orbitals of Fe and Mn. The d orbitals of Fe in the MnFe-MOF system shift to the low-energy region and the peaks become more diffused in comparison to Fe-MOF, indicating that the addition of Mn enhances Fe's stability. Simultaneously, it indicates that the addition of Mn causes the electrons of iron at the active site to be more likely to fill in the antibonding state, decreasing adsorption stability. Therefore, the lower adsorption energy of oxygen intermediates lowered the overpotential and increased the OER activity.

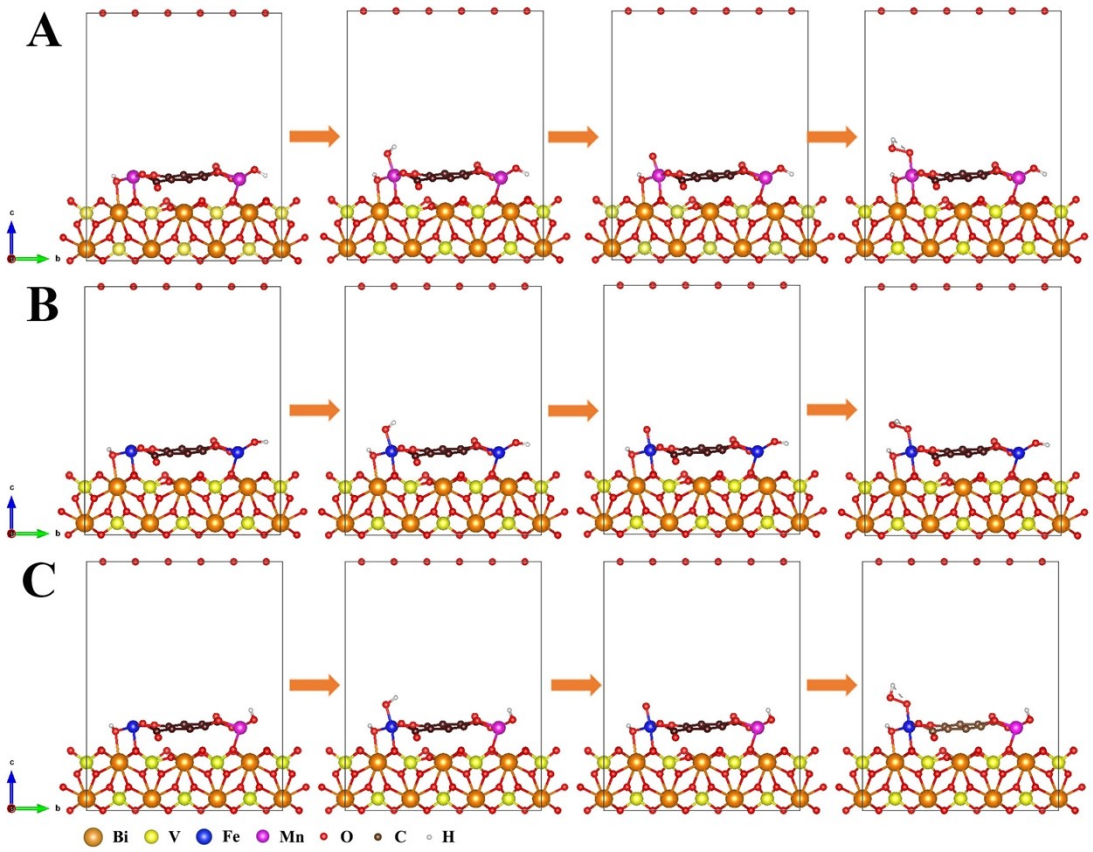

Figure S15. Construction and chemisorption models of $BiVO_4$/Mn-MOF (A), $BiVO_4$/Fe-MOF (B) and $BiVO_4$/MnFe-MOF (C) during OER process.

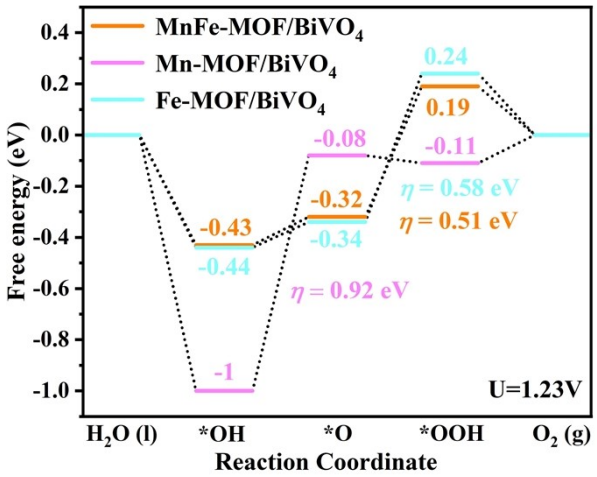

Figure S16. Gibbs free energy diagrams of $BiVO_4$/Mn-MOF, $BiVO_4$/Fe-MOF and $BiVO_4$/MnFe-MOF for OER process at U= 1.23 V.

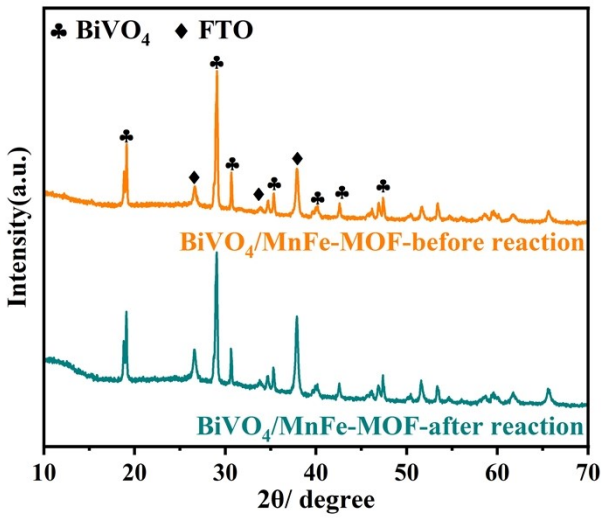

Figure S17. XRD pattern of $BiVO_4$/MnFe-MOF photoanode before and after stability test.

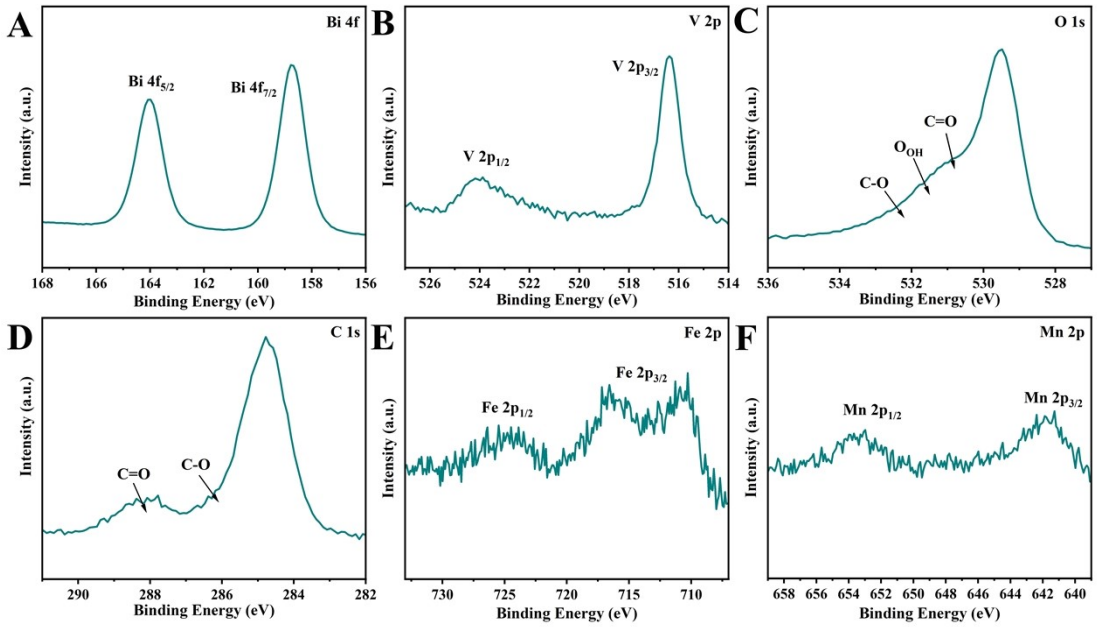

Figure S18. XPS high-resolution spectra of (A) Bi 4f, (B) V 2p, (C) O 1s, (D) C 1s, (E) Fe 2p and (F) Mn 2p for $BiVO_4$/MnFe-MOF photoanode after stability test.

Additional discussions

The XRD and XPS results of $BiVO_4$/MnFe-MOF photoanode after stability test have been exhibited in Figure S17 and 18. As illustrated in Figure S17, it can be observed that the characteristic diffraction peaks of $BiVO_4$/MnFe-MOF photoanode after stability test are essentially the same as those of the fresh samples, which should be attributed to the crystal stability of $BiVO_4$ during OER process. In addition, the high-resolution XPS spectra of the

$BiVO_4$/MnFe-MOF photoanode after stability test were shown in Figure S18. Apart from the Bi, V, and O elements of $BiVO_4$, Mn, Fe, and C elements can be also detected, thereby confirming that MnFe-MOF is not detached from the surface of $BiVO_4$ after stability test. However, an obvious decrease of C-O, C=O and O_{OH} peaks can be clearly observed in O 1s spectrum, but C 1s spectrum still exhibits apparent C-O and C=O peaks. These results suggest that long time stability test result in a poor interaction between MnFe-MOF catalysts and $BiVO_4$, which eventually leading to a slight decline of photocurrent density.

Table S1. Fitting results of Nyquist plot in Figure 5D.

sample	Rs(Ω)	CPE-P(F)	Rct(Ω)
$BiVO_4$	50.20	0.70472	1271
$BiVO_4$/Mn-MOF	40.96	0.74214	1221
$BiVO_4$/Fe-MOF	43.59	0.85404	477
$BiVO_4$/MnFe-MOF	49.07	0.84049	423

Table S2. Summary of recent significant progress of $BiVO_4$-based cocatalyst photoanodes.

Photoanodes	Photocurrent density at 1.23 V_{RHE}	ABPE	Electrolyte	Reference
$BiVO_4$/MnFe-MOF	3.64 mA cm^{-2}	1.32%	0.5M K_3BO_3	This work
CoNi-MOFs/$BiVO_4$	3.2 mA cm^{-2}	0.65%	0.5 M Na_2SO_4	6
Co-Pi/Mo:1D-BVO	3.18 mA cm^{-2}	~	0.5 M KPi	7
CoO_x/$BiVO_4$	3.36 mA cm^{-2}	0.72%	0.1 M Na_2SO_4	8
CoFeBi/$BiVO_4$	4.4 mA cm^{-2}	1.58%	0.5 M K_3BO_3	9
HT-$BiVO_4$-$NiFeO_x$	3.37 mA cm^{-2}	~1.4%	1 M K_3BO_3	10
$BiVO_4$/TAFe	3.7 mA cm^{-2}	~0.8%	0.15 M NaBi	11

BVO/Ni_2P	3.3 mA cm^{-2}	0.93%	1 M KBi	12
$BiVO_4$/CoZnNiFe-LDHs	4.0 mA cm^{-2}	1.23%	0.5M K_3BO_3	13

Reference

[1] J. Hafner, *J. Comput. Chem.*, 2008, **29(13)**: 2044-2078.

[2] P. E. Blöchl, *Phys. Rev. B*, 1994, **50(24)**: 17953.

[3] J. P. Perdew, K. Burke, M. Ernzerhof, *Phys. Rev. Lett.*, 1996, **77**, 38653868.

[4] S. Grimme, S. Ehrlich, L. Goerigk, *J. Comput. Chem.*, 2011, **32(7)**: 1456-1465.

[5] J. Anubhav, *APL Mater.*, 2013, **1**, 011002.

[6] S. Q. Zhou, K. Y. Chen, J. W. Huang, L. Wang, M. Y. Zhang, B. Bai, H. Liu, Q. Z. Wang, *Appl. Catal. B Environ.*, 2020, **266**,118513-118522.

[7] S. Zhao, H. Zhang, Z. Wang, D. Xiao, X. Xu, P. Wang, Z. Zheng, Y. Liu, Y. Dai, H. Cheng, Z. Wang, B. Huang. *CrystEngComm*, 2024, **26**, 2078-2086.

[8] M. Sui, X. Gu. *J. Electron. Mater*., 2024, 1-8.

[9] X. Zhao, Y. Rui, Y. Bai, J. Huang, H. She, J. Peng, Q. Wang. *CrystEngComm*, 2023, **25(48)**: 6677-6684.

[10] Q. Wang, L. Wu, Z. Zhang, J. Cheng, R. Chen, Y. Liu, J. Luo, *ACS Appl. Mater. Interfaces*, 2022, **14**, 26642-26652.

[11] X. Cao, C. Xu, X. Liang, J. Ma, M. Yue, Y. Ding, *Appl. Catal. B Environ.*, 2020, **260**, 118136-118144.

[12] Y. Li, Z. Li, C. Xu, S. Yu, Z. Sun, *RSC adv.*, 2023, **13(12)**: 8374-8382.

[13] C. Feng, H. Fu, X. Shao, F. Zhan, Y. Zhang, L. Wan, W. Wang, Q. Zhou, M. Liu, X. Cheng, *J. Colloid Interface Sci.*, 2024, **664**, 838-847.